Iron mineralization associated with a major strike–slip shear zone: Radiometric and oxygen isotope evidence from the Mengku deposit, NW China

Bo Wan [a,*], Wenjiao Xiao [a], Lianchang Zhang [b], Chunming Han [a]

[a] State Key Laboratory of Lithospheric Evolution, Institute of Geology and Geophysics, Chinese Academy of Sciences, P.O. Box 9825, Beijing 100029, PR China
[b] Key Laboratory of Mineral Resources, Institute of Geology and Geophysics, Chinese Academy of Sciences, P.O. Box 9825, Beijing 100029, PR China

ABSTRACT

Some skarn-associated gold deposits display close spatial relations with shear zones in ancient orogens; however to date no skarn-associated iron mineralization has been genetically linked to a shear zone. To address this problem, we conducted a systematic study of the Mengku iron deposit in the Chinese Altai, Northwest China. All orebodies of the deposit are enclosed by skarn and stratabound by volcaniclastic rocks. LA–ICP-MS dating of zircon from a meta-rhyolitic volcaniclastic (MK19) yielded a weighted $^{206}Pb/^{238}U$ age of 404 ± 5 Ma. We interpret this date as the formation time of volcanic rocks in the Mengku area, which is consistent with the age of strata hosting nearby VMS deposits (400–413 Ma). Zircon from the mineralized skarn (MK13) are considered to be hydrothermal in origin and yield a weighted $^{206}Pb/^{238}U$ age of 250 ± 2 Ma, which we interpret to represent the time of skarn formation based on the petrographic relationship between hydrothermal zircon and skarn garnet. This age is much younger than that determined from previous studies, younger than the regional igneous and metamorphism activities (early Permian), but synchronous with the movement of the nearby regional Erqis shear zone and Abagong Fault (late Permian to Triassic). The oxygen isotope values of the hydrothermal zircon are 2.3‰ to 3.0‰, consistent with the $\delta^{18}O$ of garnet (1.2‰ to 3.2‰) in the skarn, but markedly different from those of zircon from igneous rocks in the mine area (MK1, 2, 3, 19; 6.3‰ to 8.0‰). The fluid source has a strong meteoric water signature as indicated by the oxygen isotope values of garnet and hydrothermal zircon, which are very different from those of the granite and volcanic rocks in the mine area. On the basis of field, chronological and geochemical evidence, we suggest that the Mengku is not a volcanogenic massive sulfide deposit, but is related to the Erqis strike–slip shear zone and Abagong Fault, which acted as fluid conduits. The upwelling of hot mantle in the Permian to Triassic supplied the heat, and thereby caused material to dehydrate and mixed with meteoric water that give rise to low-oxygen isotope fluids similar to the common genetic model for orogenic lode gold deposits.

1. Introduction

Most economic skarn deposits form via metasomatism of country rocks surrounding plutons, where the latter provide for hydrothermal fluids and are a source of the ore metals (e.g., Ciobanu and Cook, 2004; Maher, 2010; Meinert et al., 1997; Pons et al., 2009). Many studies have concentrated on the geochemical properties of the intrusions and on the question whether specific magma sources are required to form economically significant deposits of Fe, Cu, Mo, W, Sn, Zn and Au (Meinert et al., 2005, and reference therein). However, skarns can also form in many other different environments as seafloor hydrothermal vents (Doyle and Allen, 2003) or deeply-buried metamorphic terranes (Mueller, 1997). Many skarn deposits in ancient orogens do not have a clear link with their host intrusive. Instead, they may be stratabound within specific lithological units as in Nuuk in West Greenland, the

Austroalpine Alps and the Lower Yangtze River Valley in China (Appel, 1994; Einaudi et al., 1981; Gu et al., 2007; Raith and Stein, 2000, respectively). In such cases, their genesis is usually interpreted as either the result of seafloor exhalation or of regional metamorphism, less commonly as an intrusion-related mineral system.

Skarns also occur along faults and major shear zones (Leloup and Kienast, 1993), and in some cases, skarn mineralization can be placed in similar structural contexts (Bullis et al., 1994). However no skarn-associated iron deposit has ever been genetically linked to a specific shear zone. Shear zones can be channels for large-scale fluid movements, and are characterized by a wide temperature range (200 to 650 °C) range (Groves et al., 2003). The main question is whether shear zones can generate economically significant iron deposits, and to address this problem we carried out a systematic study of the Mengku iron deposit in Xinjiang, the largest iron deposit in the NW China (220 Mt Fe). Hydrothermal zircon from mineralized skarns were separated and dated via LA–ICP-MS, with oxygen isotope analysis of zircon from the skarn and volcanic wallrocks and intrusions in the mine area carried out via SIMS.

This data has allowed us to build a spatial and temporal relationship between iron mineralization and a major shear-zone, based on field observations, isotope dating, and source tracing, allowing us to propose a new model for the genesis of the Mengku iron deposit.

2. Geological background

2.1. Regional geology

The Altaids is composed of a number of accretionary collages recording a long-lived accretionary history from ca. 650 Ma to 250 Ma, and it represents the largest Phanerozoic continental growth on Earth (Kröner et al., 2007; Şengör et al., 1993; Windley et al., 2007; Xiao et al., 2010). It is bound by the Siberian Craton to the north, and the Tarim and North China cratons to the south (Fig. 1, inset; Allen et al., 1993; Cunningham et al., 1996; Şengör et al., 1993; Zonenshain et al., 1990). At present, there is no consensus on the development of the entire accretionary orogenesis (Charvet et al., 2007; Şengör and Natal'in, 1996; Xiao et al., 2009a), but detailed geological information of some units have been well documented for the Chinese Altai–East Junggar collage in Northwest China (Wan et al., 2011; Xiao et al., 2009a). This collage is located between the northern and southern boundaries of the Altaids, straddling the international borders of China, Kazakhstan, and Russia (Fig. 1, inset). The Chinese Altai consists of Cambrian to Carboniferous calc-alkaline volcanic rocks and sedimentary rocks (Long et al., 2007, 2010; Sun et al., 2008; Wang et al., 2009a), and two granitoid suites were emplaced at 408 to 377 Ma and 344 to 290 Ma (Chen and Jahn, 2004; Jahn et al., 2000; Wang et al., 2006; Yuan et al., 2007).

The Chinese Altai underwent regional metamorphism starting with kyanite-grade metamorphism related to burial history, followed by andalusite-grade as a result of late magmatism and fluid activities in the exhumation stage (Wang et al., 2009b; Wei et al., 2007; Zheng et al., 2007). East Junggar is dominated by Ordovician to Carboniferous calc-alkaline volcanic rocks with minor sediments (Chen and Jahn, 2004; Niu et al., 2006), and is characterized by greenschist facies

metamorphism (Wei et al., 2007). The Chinese Altai and East Junggar orogens are interpreted to represent two independent island arcs formed by northward subduction from the early to late Paleozoic, then laterally accreted together in the Carboniferous along the Erqis (also Irtysh or Ertix) shear zone in the north (present coordinates) during final closure of the Paleo-Asian ocean (Fig. 1; Xiao et al., 2009b). Many oblique thrusts in the Chinese Altai are the result of lateral accretion between these two arcs (Qu and Zhang, 1994).

The Erqis shear zone represents the largest fault in Asia and extends NW–SE for more than 1000 km, has a 10–15 km-wide mylonitic zone, and contains numerous gold and mercury deposits (Windley et al., 2002). The activation time of the fault has been recently constrained at 278 ± 9 Ma to 200 ± 2 Ma by high resolution Th–Pb and Ar–Ar methods (Briggs et al., 2007; Briggs et al., 2009). On both sides of the shear zone there are many types of ore deposits, including VMS copper–lead–zinc deposits, orogenic lode gold, iron ore deposits in the Chinese Altai (Wan et al., 2010a; Xu et al., 2008), and porphyry Cu–Mo deposits in East Junggar (Wan et al., 2011). Most researchers attributed the formation of these deposits to subduction-related processes (Goldfarb et al., 2003; Rui et al., 2002). The present work on the Mengku iron deposit demonstrates that it cannot fall into this geodynamic framework.

2.2. Deposit geology

The Mengku iron deposit in Xinjiang Province, Northwest China, is structurally located on the northern limb of a giant overturned syncline (the Maizi basin) in the southern Chinese Altai; the synclinal axial plane dips NE and strikes NW–SE. The 3 km^2 iron deposit is bordered by the Abagong thrust fault in the north, and is associated with the Silurian Kulumuti Group, the Lower Devonian Kangbutiebao Formation and three types of granite (Fig. 2).

The Kulumuti Group is composed of schist and meta-siltstone, which crop out in the northwest in the mine area. The Kangbutiebao Formation is exposed in the southern Chinese Altai, and is the main host of the iron
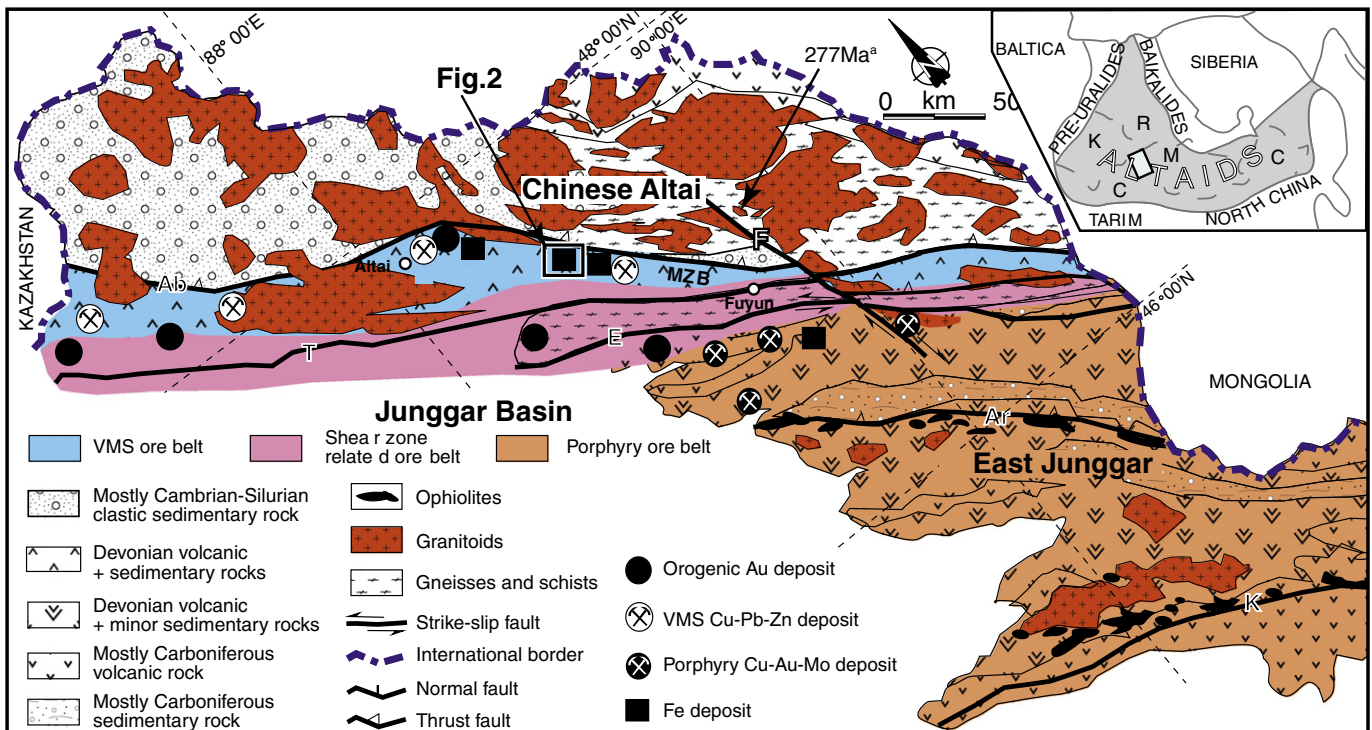

Fig. 1. Geological map of the Chinese Altai Orogen showing the main units and ore deposits (modified from Wan et al., 2010b). The location of Fig. 2 is marked. MZB — Maizi Basin; Ab — Abagong Fault; T — Tesibahan Fault; E — Erqis shear zone; Ar — Armantai Fault; K — Kelamaili Fault; F — Fuyun Fault. The age marked as 'a' is from Wang et al. (2007).
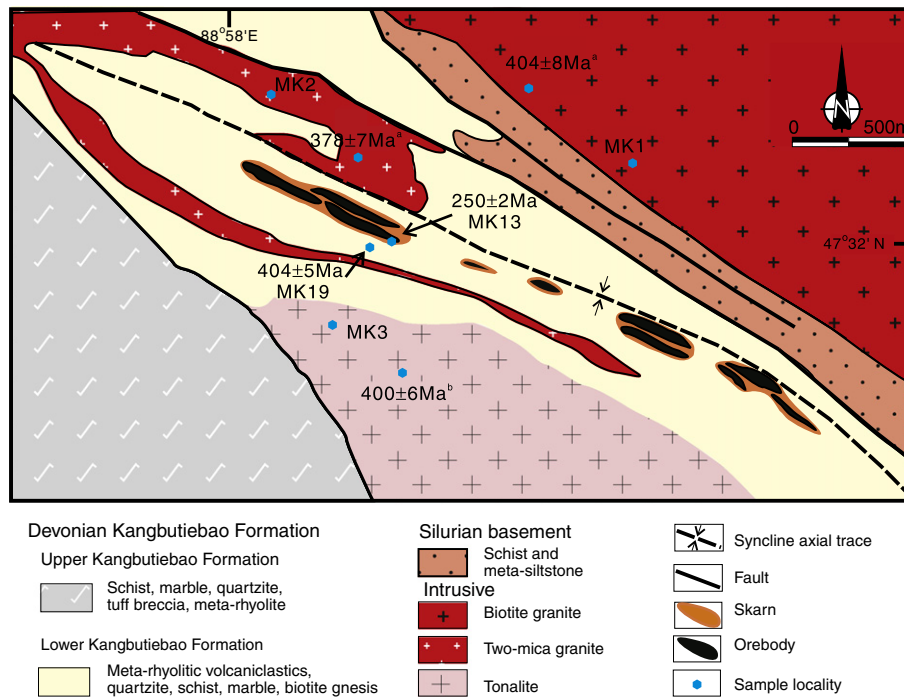
Fig. 2. Geologic map of the Mengku iron deposit modified from FGTBGMRX (2005). The age marked as 'a' is from Xu et al. (2010), 'b' from Yang et al. (2010).

ore at Mengku. It consists of meta-rhyolitic volcaniclastics, meta-sedimentary rocks, and minor mafic volcanic rocks, and is divisible into Upper and Lower parts based on different fossils in the sedimentary rocks (Fourth Geological Team of Bureau of Geology and Mineral Resources of Xinjiang (FGTBGMRX), 2005). Most of the exposed strata at the Mengku iron deposit belong to the Lower Kangbutiebao Formation, which consists of meta-rhyolitic volcaniclastics, quartzite, schist, marble and biotite gneiss (FGTBGMRX, 2005). The Upper Kangbutiebao Formation comprises schist, marble, meta-sandstone, tuff breccia and meta-rhyolitic volcaniclastics. U–Pb zircon ages of host volcaniclastics of different deposits include: 401 ± 3 Ma (SIMS U–Pb for a VMS deposit; Liu et al., 2010; Wan et al., 2011), 413 ± 4 Ma, 409 ± 5 Ma, 407 ± 4 Ma (SHRIMP U–Pb for a iron deposit; Chai et al., 2009), and an early Devonian age has been proposed for the Kangbutiebao Formation.

Intrusive rocks crop out extensively in the mine area (Fig. 2), and all these granites intrude the Kangbutiebao Formation. Biotite granite and tonalite are distributed in the northeast and south of the mine area (Fig. 2), with emplacement ages of 404 ± 8 Ma and 400 ± 6 Ma respectively (SHRIMP U–Pb; Xu et al., 2010; Yang et al., 2010). These two ages are similar within error, and probably represent the first intrusive event in the mine area. Two slices of two-mica granite with an emplacement age of 378 ± 7 Ma (SHRIMP U–Pb; Xu et al., 2010), crop out in the center and west of the mine area (Fig. 2).

Many orebodies are aligned along the axis of a syncline in the mine (Fig. 2), and nine of them account for 90% of the total reserves. The orebodies strike NW and dip 80° NE, are lenticular in shape and are surrounded by meta-rhyolitic volcaniclastic rocks. Textures of the ore range from massive, banded, disseminated and irregular. Magnetite is the dominant iron-bearing ore mineral, and occurs with pyrrhotite, pyrite and chalcopyrite. Gangue minerals include diopside, amphibole, garnet, actinolite, chlorite, epidote, quartz, calcite and other calc-silicate minerals.

At the Mengku mine each orebody is enclosed by a calc-silicate mineral assemblage interpreted as skarn, and both the skarn and ore therein are broadly stratabound by meta-rhyolitic volcaniclastic rocks. However one skarn clearly cuts across a fold (Fig. 3a), indicating that at least some skarn body formation postdated deformation of the host

rock, and such a structural relationship can be observed in many places in the mine area. Granite crops out at the Mengku deposit, however no skarn occurs at the contact between granite bodies and volcanic and sedimentary rocks. In addition, a drill core contains no evidence of direct or transitional contacts between skarn and granites (FGTBGMRX, 2005).

3. Sample description, analytical methods and results

3.1. Sample description

The skarn contains variable proportions of garnet, diopside, epidote and amphibole with at least two kinds of garnet: one fine-grained (<0.2 mm) and the other coarse-grained (up to 5 cm), occurring with calcite veins. All diopside and epidote are fine-grained. The skarn is zoned at outcrop scale, with a core red garnet skarn (garnet more abundant than diopside), enveloped by dark green diopside skarn, coated by an outermost epidote skarn (Fig. 3a). Spatially, the magnetite ores are mostly associated with the garnet skarn, less so with diopside skarn, and almost absent in the epidote skarn. Zircon grains were separated from two samples, one from a mineralized skarn (MK13), and the other from a barren meta-rhyolitic volcaniclastic rock (MK19). Sample locations are indicated in Fig. 2. Sample MK13 consists of 50% modal garnet, 30% modal diopside, 15% modal magnetite, quartz and calcite. Accessory minerals like zircon can be observed in garnet (Fig. 3b), and garnet crystals can be also found in zircon (Fig. 3c). Sample MK19, collected from meta-rhyolitic volcaniclastic rocks in the vicinity of No. 6 orebody, is mainly composed of recrystallized quartz and feldspar that are hydrothermally unaltered.

3.2. Analytical methods

Zircon grains from MK 1, 2, 3, 13, and 19 were separated via a combination of heavy liquid and magnetic techniques, then mounted in epoxy resin and polished to remove the upper one third of the grains. Cathodoluminescence (CL) images were obtained based on LEO1450VP SEM by Mini CL detector in order to identify internal
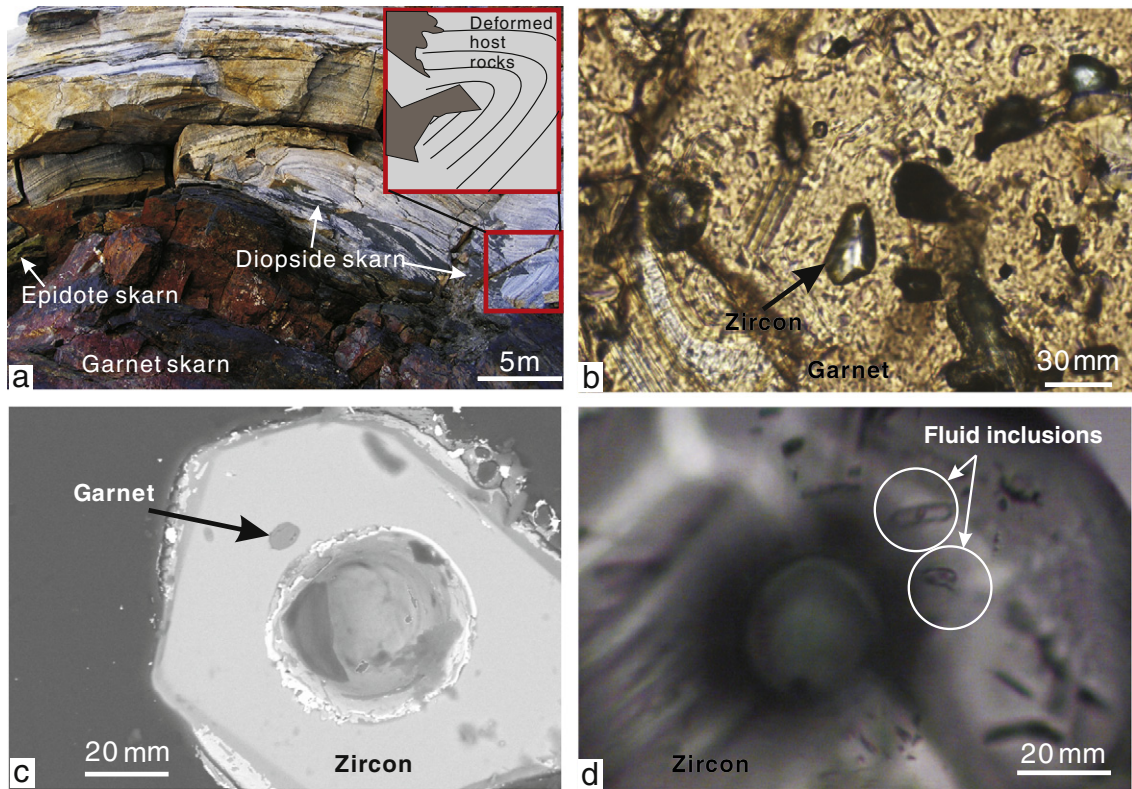
Fig. 3. (a) Dark gray polygons in the inset represent a skarn that cross-cuts a fold in host rhyolitic volcaniclastic rocks, and a small-scale skarn zonation can be distinguished from the core of a garnet skarn to the outermost zone of an epidote skarn; (b) zircon in garnet; (c) garnet inclusion in zircon; (d) Fluid inclusions in zircon from the mineralized skarn.

structures and choose potential target sites for U–Pb and O analyses. Under a single-polarized microscope, most zircon crystals from MK13 have primary fluid inclusions (Fig. 3d), and are irregular in shape. Zircon separated from MK1 (biotite granite), MK2 (two-mica granite), MK3 (tonalite) and MK19 are prismatic and are oscillatory zoned under CL (Fig. 4). Isotopic measurements were carried out in the MC–ICPMS laboratory of the Institute of Geology and Geophysics, Chinese Academy of Sciences (IGGCAS) in Beijing. An Agilent 7500a quadruple (Q)-ICPMS was used for simultaneous determination of zircon U–Pb age, trace elements with a 193 nm excimer ArF laser-ablation system (GeoLas Plus) attached. Detailed analytical procedures and experimental parameters are described by Xie et al. (2008), only an outline is given here.

Before analysis, the sample surface was cleaned with ethanol to eliminate possible contamination. Every five sample analyses were followed by analyzing of a suite of zircon standards: zircon 91500 (Wiedenbeck et al., 1995), Gj-1(Jackson et al., 2004) and NIST SRM 610. Each spot analysis consisted approximately of 30 s background acquisition and 40 s sample data acquisition. During experiments, the laser parameters-spot size was set to 44 μm, with frequency of 8 Hz and fluence of 15 J/m^2. The ablation material was sent to the Q-ICPMS for U–Pb isotopic and trace elemental analyses. $^{207}Pb/^{206}Pb$, $^{206}Pb/^{238}U$, $^{207}U/^{235}U$ ($^{235}U = ^{238}U/137.88$), $^{208}Pb/^{232}Th$ ratios were corrected by using zircon 91500 as an external standard. Zircon Gj-1 was an unknown sample and yielded a weighted mean $^{206}Pb/^{238}U$ age of 603 ± 5 Ma (2σm, MSWD = 0.1, n = 50), which is in good agreement with the recommended U–Pb age (Jackson et al., 2004). The relative standard deviations of reference values for 91500 were set at 2%. The fractionation correction, $^{207}Pb/^{206}Pb$ and $^{206}Pb/^{238}U$ ratios were calculated using GLITTER 4.0 (Griffin et al., 2008). Common Pb was corrected according to the method proposed by Andersen (2002). The weighted mean U–Pb ages and concordia plots were processed using ISOPLOT 2.3 (Ludwig, 2001). ^{40}Si was used as an internal standard for trace element. NIST SRM 610 was used as an external standard for trace element.

Zircon oxygen isotopes were obtained with a Cameca IMS 1280 large-radius SIMS at IGGCAS. Detailed analytical procedures can be found in Li et al. (2009) and Li et al. (2010), and only brief conditions are given here. The Cs + primary beam was accelerated at 10 kV with an intensity of ca. 2 nA. The spots size was approximately 20 μm in diameter, and secondary ions were extracted with a −10 kV potential. Oxygen isotopes were measured in multi-collector mode with two off-axis Faraday cups with each analysis consisting of 20 cycles × 4 s counting time. The instrumental mass fractionation factor was corrected using 91500 zircon standard with $\delta^{18}O$ VSMOW = 9.9‰ (Wiedenbeck
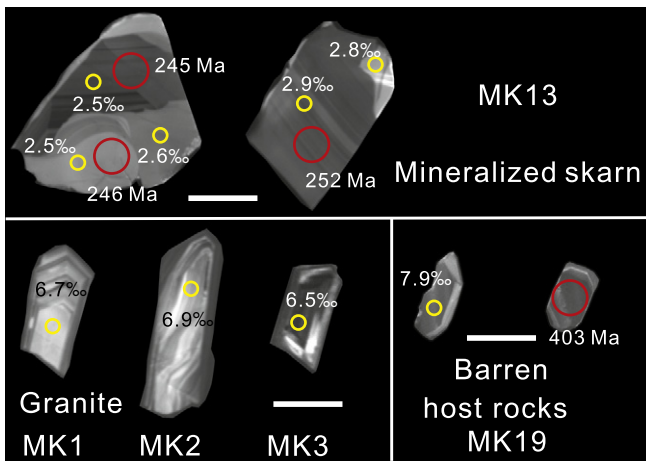

Fig. 4. Representative cathodoluminescence (CL) images of zircons. Large red circles represent the location of geochronological points and small yellow circles represent oxygen measurement points. White bar is 100 μm.

et al., 1995). Point-to-point uncertainty was typically better than 0.4‰ (2 SD) for δ^{18}O. Measurements of the TEMORA2 zircon standard during the course of this study yielded a weighted mean of δ^{18}O = 8.1 ± 0.2‰ (n = 10, 2σm), which is consistent within errors with the reported value of 8.2‰ (Black et al., 2004). Garnet oxygen compositions were determined on a Finnigan-MAT252 mass spectrometer at IGGCAS. Oxygen was extracted from garnet by the BrF method (Clayton and Mayeda, 1963). The analytical precisions were ± 0.1‰.

Garnet compositions were determined at IGGCAS using a JEOL JXA-8100 electron microprobe. The operating conditions were in wavelength-dispersive (WDS) mode. Analyses were undertaken employing a 1–2 μm beam spot size, with 15 kV accelerating voltage, counting time of 20 s and 20 nA beam current per element. Microprobe analytical standards were jadeite for Na, Al, and Si, olivine for Mg, synthetic chromite for Cr, chrome diopside for Ca, orthoclase for K, rutile for Ti, rhodonite for Mn, and garnet for Fe. A program based on the ZAF procedure was used for data correction.

3.3. Results

Measured U–Pb isotopic ratios and trace element concentrations are presented in Table 1. We analyzed twenty-three spots on twenty-two grains for MK13, all results yielded two age populations, twenty-one of them had a weighted mean ^{206}Pb/^{238}U age of 250 ± 2 Ma (95% confidence limits, MSWD of 0.9), and the other two had a weighted age of ca. 404 ± 12 Ma. One grain from MK13 shows irregular zonations, and analytical spots on different domains yield age of ca. 250 Ma (Fig. 4). All grains with younger ages are characterized by low Th/U ratios (<0.1), with the older two recording high Th/U ratios of 0.65 and 0.7. In sample MK19, fifteen grains yield ages between 393 and 422 Ma, with a mean weighted age of 404 ± 5 Ma and MSWD of 1.4 (Fig. 5). Th/U ratios for these zircon range between 0.48 and 0.96.

Measured O isotopic ratios are listed in Table 2 and depicted in Fig. 6. Twenty analyses of O isotope ratio on zircon from sample MK13 yielded δ^{18}O‰ of 2.4‰–3.0‰. Although some zircon grains from MK13 show irregular domains, these zircons are homogeneous with regard to oxygen isotopes (Fig. 4). Oxygen isotopic data of garnet from the mineralized skarn consistently yield δ^{18}O‰ values of 1.2‰–3.2‰. The oxygen isotopes of the minerals from skarn (garnet and zircon) are distinctive from those from host rocks and intrusions. For example, zircons from sample MK 19 yield δ^{18}O‰ values of 7.0‰–8.0‰, whereas those from samples MK1, MK2 and MK3 are essentially the same, ranging from 6.4‰ to 7.7‰, 6.4‰–7.8‰ and 6.3‰–7.5‰ respectively.

Table 1
U–Pb isotope and trace elemental data of zircon from the mineralized skarn and barren country rock of the Mengku iron deposit.

| No	Isotopic ratios						Age (Ma)						Concentration (ppm)		
	$\frac{^{207}Pb}{^{206}Pb}$	1σ	$\frac{^{207}Pb}{^{235}U}$	1σ	$\frac{^{206}Pb}{^{238}U}$	1σ	$\frac{^{207}Pb}{^{206}U}$	1σ	$\frac{^{207}Pb}{^{235}U}$	1σ	$\frac{^{206}Pb}{^{238}U}$	1σ	Th	U	Th/U
MK13 from the mineralized skarn															
1	0.0512	0.0009	0.2795	0.0045	0.0396	0.0007	248	18	250	4	251	4	37	943	0.04
2	0.0512	0.0018	0.2720	0.0086	0.0386	0.0008	248	36	244	7	244	5	27	889	0.03
3	0.0509	0.0008	0.2756	0.0040	0.0393	0.0007	235	18	247	3	248	4	43	879	0.05
4	0.0501	0.0007	0.2729	0.0034	0.0395	0.0007	201	19	245	3	250	4	17	1155	0.01
5	0.0518	0.0008	0.2841	0.0038	0.0398	0.0007	277	18	254	3	251	4	51	985	0.05
6	0.0537	0.0017	0.4851	0.0140	0.0655	0.0013	360	31	402	10	409	8	140	216	0.65
7	0.0496	0.0009	0.2788	0.0047	0.0408	0.0007	177	19	250	4	258	5	44	933	0.05
8	0.0507	0.0007	0.2792	0.0036	0.0399	0.0007	229	19	250	3	252	4	49	1182	0.04
9	0.0512	0.0009	0.2847	0.0045	0.0403	0.0007	252	18	254	4	255	4	18	1495	0.01
10	0.0499	0.0006	0.2720	0.0027	0.0396	0.0007	188	21	244	2	250	4	46	1014	0.05
11	0.0508	0.0007	0.2781	0.0032	0.0397	0.0007	233	20	249	3	251	4	95	2349	0.04
12	0.0507	0.0016	0.2787	0.0079	0.0399	0.0008	228	31	250	6	252	5	42	904	0.05
13	0.0512	0.0013	0.2738	0.0065	0.0388	0.0008	248	25	246	5	246	5	41	977	0.04
14	0.0501	0.0008	0.2789	0.0042	0.0404	0.0007	200	18	250	3	255	4	28	1227	0.02
15	0.0514	0.0014	0.2750	0.0066	0.0389	0.0008	257	25	247	5	246	5	162	579	0.28
16	0.0511	0.0018	0.2727	0.0087	0.0387	0.0009	244	36	245	7	245	5	32	398	0.08
17	0.0510	0.0009	0.2718	0.0046	0.0387	0.0007	239	19	244	4	245	4	46	497	0.09
18	0.0519	0.0016	0.2936	0.0083	0.0410	0.0009	281	30	261	6	259	6	44	507	0.09
19	0.0512	0.0011	0.2855	0.0058	0.0405	0.0008	248	21	255	5	256	5	162	585	0.28
20	0.0510	0.0008	0.2793	0.0041	0.0397	0.0007	240	19	250	3	251	5	37	479	0.08
21	0.0548	0.0022	0.4809	0.0181	0.0635	0.0016	404	42	398	12	397	10	380	546	0.70
22	0.0507	0.0010	0.2708	0.0048	0.0388	0.0007	225	20	243	4	245	5	23	327	0.07
23	0.0511	0.0012	0.2719	0.0060	0.0386	0.0008	244	23	244	5	244	5	26	379	0.07
MK19 from barren meta-rhyolitic volcaniclastics															
1	0.0559	0.0024	0.5072	0.0194	0.0659	0.0017	447	42	417	13	411	10	347	432	0.80
2	0.0538	0.0007	0.4948	0.0060	0.0667	0.0012	361	21	408	4	416	7	470	532	0.88
3	0.0544	0.0023	0.4797	0.0185	0.0639	0.0016	387	44	398	13	399	10	332	494	0.67
4	0.0568	0.0012	0.4932	0.0094	0.0629	0.0012	484	20	407	6	393	8	460	626	0.73
5	0.0564	0.0012	0.4891	0.0094	0.0629	0.0012	468	20	404	6	393	8	190	310	0.61
6	0.0541	0.0014	0.4824	0.0116	0.0646	0.0013	377	24	400	8	403	8	562	586	0.96
7	0.0541	0.0011	0.4831	0.0086	0.0648	0.0013	374	19	400	6	405	8	250	321	0.78
8	0.0538	0.0022	0.4806	0.0181	0.0648	0.0017	361	42	399	12	405	10	295	382	0.77
9	0.0561	0.0007	0.5234	0.0059	0.0676	0.0012	457	21	427	4	422	7	486	742	0.65
10	0.0541	0.0008	0.4827	0.0067	0.0647	0.0012	376	20	400	5	404	7	148	309	0.48
11	0.0558	0.0014	0.5142	0.0115	0.0668	0.0014	445	22	421	8	417	8	232	342	0.68
12	0.0554	0.0017	0.4966	0.0138	0.0649	0.0015	430	28	409	9	406	9	444	482	0.92
13	0.0566	0.0014	0.4992	0.0113	0.0640	0.0012	476	22	411	8	400	7	140	216	0.65
14	0.0545	0.0017	0.4773	0.0138	0.0636	0.0013	390	31	396	9	397	8	201	303	0.66
15	0.0546	0.0011	0.4781	0.0090	0.0635	0.0008	395	21	397	6	397	5	481	637	0.76

1σ refers to the absolute error.
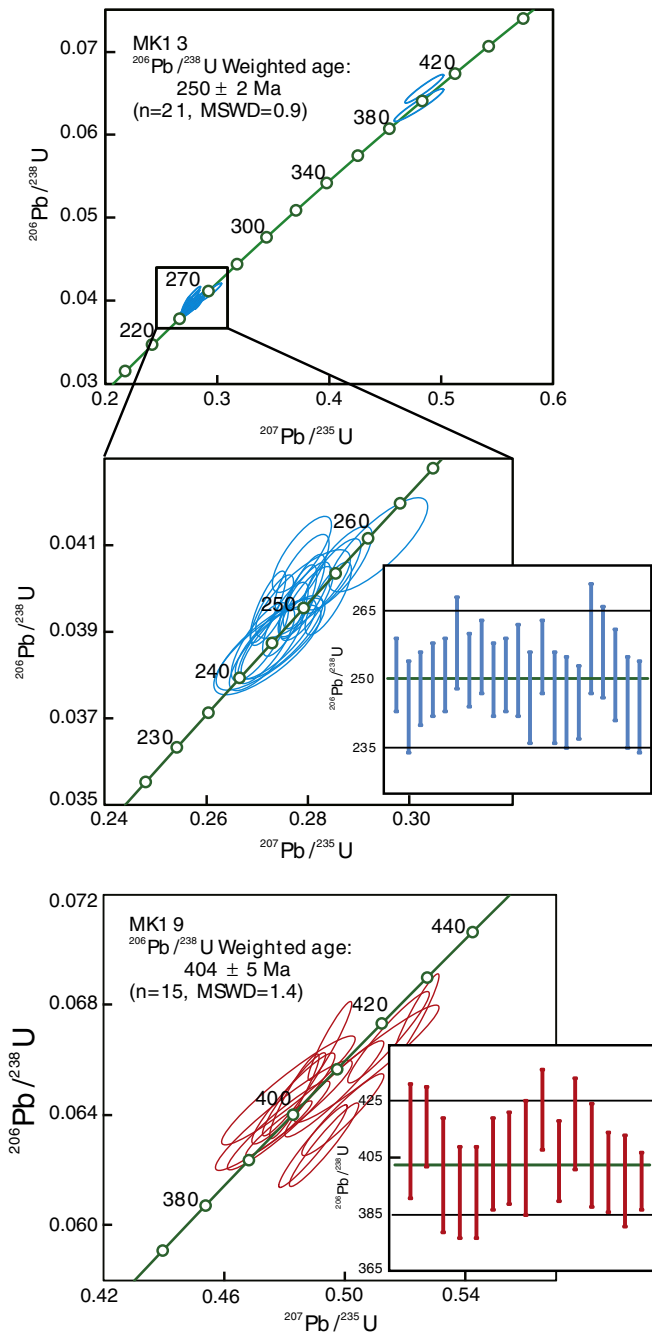
Fig. 5. U–Pb concordia diagrams for hydrothermal zircons from skarn and magmatic zircon populations from host meta-rhyolitic volcaniclastics.

All garnet in the Mengku deposit are calcium-rich garnet in compositions, mainly composed of andradite and grossular (>90%; Fig. 7). The mineral inclusion in zircon in Fig. 3c was confirmed via the microprobe as andraditic garnet. All analytical results are listed in Table 3.

4. Discussion

4.1. Genetic implications of zircon growth and recorded mineralization ages

Zircon from the meta-rhyolitic volcaniclastic sample (MK19) is euhedral and characterized by oscillatory zonations that indicate magmatic growth (Hoskin and Schaltegger, 2003). Although all rocks in the area underwent low-grade metamorphism, the zircon preserves no evidence of disturbance of the U–Pb system, with all analyses yielding a simple age population of 404 ± 5 Ma. The Th/U ratios of these

zircons are 0.48 to 0.96, indicating a magmatic origin (Hoskin and Schaltegger, 2003). The oxygen isotopic ratios are from 7.0‰ to 8.0‰, a range that is very similar to magmatic $\delta^{18}O$‰ values (e.g., Valley, 2003). This evidence clearly indicates that zircon from the meta-rhyolitic volcaniclastic rocks is magmatic, and their age represents the time of formation of the volcaniclastic rocks. There are many VMS deposits in the Chinese Altai with ore host rock ages ranging from 401 ± 3 Ma to 413 ± 4 Ma (Chai et al., 2009; Liu et al., 2010; Wan et al., 2011). The similarity between the age we obtained and the published ages suggests that the meta-rhyolitic volcaniclastic rocks in the Mengku deposit are similar to those that host the VMS deposits.

Most zircon from the mineralized skarn (MK13) displays anhedral texture. Twenty-one analytical spots on twenty grains yield a weighted $^{206}Pb/^{238}U$ age of 250 ± 2 Ma and low Th/U ratios (<0.1). The low Th/U ratio may result from a much lower solubility of Th over U in an aqueous fluid (Johnson and Plank, 1999). Abundant primary fluid inclusions in these younger grains are evidence that they formed in an aqueous fluid-rich environment (Fig. 3d). The oxygen isotope ratios of these hydrothermal zircons (2.4‰–3.0‰) indicate that they are characterized by a strong signature of meteoric water (Wilde et al., 2001). We interpreted the low Th/U ratio, abundant fluid inclusions and distinct oxygen isotope signature as evidence of growth of these zircon from a hydrothermal fluid (Hoskin, 2005; Hoskin and Schaltegger, 2003). As shown in Fig. 6, zircon from MK13 is distinct from those in the host rocks (MK19) and intrusions (MK1, 2, 3) in the Mengku mine area, both in terms of their age and oxygen isotopes, indicating that they formed from different sources. In addition, the oxygen isotope ratio of hydrothermal zircon is indistinguishable of that of garnet (1.2‰ to 3.2‰) separated from the skarn, suggesting that both formed contemporaneously from the same source. In thin section, zircon is enclosed by garnet (Fig. 3b); and garnet occurs as a mineral inclusion in hydrothermal zircon (Fig. 3c). This relationship suggests that garnet and zircon crystallized almost simultaneously; therefore we interpreted the age of the hydrothermal zircon dated in this study as the time of skarn formation. Most workers have suggested that the skarn formed a little earlier than the magnetite ore (Wang et al., 2003; Xu et al., 2010; Yang et al., 2008), therefore, the skarn age can predate or almost represent the mineralization age. The zircon age of 250 ± 2 Ma is the age of skarn, which can be interpreted as the time of the iron mineralization. From the mineralized skarn, some zircon preserved older age of ca. 400 Ma. We suggest that this zircon may be inherited from the skarn host rocks, and records the time of formation of the rhyolitic volcaniclastics.

4.2. Implications for ore genesis

In general, skarns form during regional or contact metamorphism via a variety of metasomatic processes involving fluids of magmatic, metamorphic, meteoric, and/or marine origin (see Meinert et al., 2005 and references therein), and consequently the formation of skarn mineral deposits can be complicated. Two competing models have been proposed to explain the origin of the Mengku deposit: a distal iron-rich orebody of VMS-type (Wang et al., 2003), and a granite-related skarn deposit (Xu et al., 2010; Yang et al., 2010). Both models assume that skarn formation was synchronous with volcanism and granite formation. The following sections evaluate and test these two models in detail with our new geological, geochemical and chronological results.

4.2.1. A distal iron-rich portion of a VMS deposit?

According to the distal iron-rich VMS model, a skarn forms by reaction between hydrothermal fluids and sub-seafloor rocks (Wang et al., 2003). The VMS model provides an explanation for the fact that all the orebodies are stratabound and hosted by volcanic rocks. Skarn minerals are common in VMS deposits, and it is usual to find skarns in the footwall or hanging wall of a concordant orebody, typically proximal to some hydrothermal vents (Doyle and Allen, 2003). Skarn minerals

Table 2
Oxygen isotope ratio of garnet and zircon from Mengku iron deposit.

No.	Mineral	δ¹⁸O ‰ VSMOW	σ	No.	Mineral	δ¹⁸O ‰ VSMOW	σ	No.	Mineral	δ¹⁸O ‰ VSMOW	σ
From mineralized skarn				MK2	Zircon	7.5	0.2	MK13	Zircon	2.5	0.2
MK5-A	Garnet	1.4	0.1	MK2	Zircon	7.6	0.3	MK13	Zircon	3.0	0.3
MK5-B	Garnet	2.1	0.2	MK2	Zircon	7.1	0.3	MK13	Zircon	2.5	0.2
MK5-C	Garnet	1.2	0.1	MK2	Zircon	7.5	0.3	MK13	Zircon	2.6	0.3
MK5-D	Garnet	1.6	0.2	MK2	Zircon	7.8	0.4	MK13	Zircon	2.7	0.4
MK5-E	Garnet	2.8	0.3	MK2	Zircon	7.6	0.2	MK13	Zircon	2.6	0.4
MK5-F	Garnet	2.7	0.3	From tonalite				MK13	Zircon	2.3	0.3
MK5-G	Garnet	3.2	0.3	MK3	Zircon	6.3	0.4	MK13	Zircon	2.0	0.2
MK5-H	Garnet	2.0	0.2	MK3	Zircon	6.7	0.3	MK13	Zircon	2.7	0.3
From biotite granite				MK3	Zircon	7.5	0.4	MK13	Zircon	2.5	0.2
MK1	Zircon	6.5	0.3	MK3	Zircon	6.5	0.2	MK13	Zircon	2.6	0.4
MK1	Zircon	7.4	0.3	MK3	Zircon	7.0	0.3	MK13	Zircon	2.7	0.4
MK1	Zircon	7.5	0.3	MK3	Zircon	6.9	0.3	MK13	Zircon	2.8	0.3
MK1	Zircon	7.1	0.3	MK3	Zircon	6.6	0.4	From host volcaniclastics			
MK1	Zircon	7.7	0.4	MK3	Zircon	6.8	0.3	MK19	Zircon	7.8	0.4
MK1	Zircon	6.6	0.3	MK3	Zircon	6.5	0.3	MK19	Zircon	7.5	0.2
MK1	Zircon	6.7	0.3	MK3	Zircon	6.3	0.3	MK19	Zircon	7.7	0.2
MK1	Zircon	6.4	0.1	MK3	Zircon	7.3	0.4	MK19	Zircon	7.2	0.2
MK1	Zircon	6.7	0.3	MK3	Zircon	6.5	0.3	MK19	Zircon	7.5	0.3
MK1	Zircon	6.9	0.2	MK3	Zircon	6.8	0.4	MK19	Zircon	7.9	0.2
MK1	Zircon	7.3	0.4	From mineralized skarn				MK19	Zircon	7.4	0.3
From two-mica granite				MK13	Zircon	2.5	0.3	MK19	Zircon	7.5	0.3
MK2	Zircon	6.5	0.3	MK13	Zircon	2.6	0.2	MK19	Zircon	8.0	0.3
MK2	Zircon	6.5	0.2	MK13	Zircon	2.4	0.3	MK19	Zircon	7.4	0.4
MK2	Zircon	6.4	0.3	MK13	Zircon	2.7	0.2	MK19	Zircon	7.7	0.2
MK2	Zircon	6.7	0.3	MK13	Zircon	2.9	0.3	MK19	Zircon	7.7	0.3
MK2	Zircon	7.5	0.3	MK13	Zircon	2.4	0.3	MK19	Zircon	7.8	0.7
MK2	Zircon	6.9	0.4	MK13	Zircon	2.4	0.4	MK19	Zircon	7.0	0.4

1σ refers to the absolute error.

surround the iron orebody in the Mengku deposit, which is uncommon in VMS deposits. More importantly, it is widely considered that VMS deposits are syn-volcanic (Franklin et al., 2005), but our new zircon age of the skarn (250 Ma) is significantly younger than that of the host meta-rhyolitic volcaniclastic rocks (ca. 400 Ma). This is supported by field observations, where the Mengku skarn cross-cuts a fold in the host meta-rhyolitic volcaniclastics (Fig. 3a), indicating that the skarn formed later than the deformation. We interpret the younger age and this cross-cutting relationship to exclude the possibility that the skarn is a syn-volcanic product. In addition, the garnet composition at the Mengku ore is different from that of typical VMS deposits both in the Chinese Altai (Liu et al., 2010) and elsewhere (Gemmell et al., 1992). The Mengku garnet is Ca-rich (90% andradite + grossular), whereas garnet associated with other VMS deposits is predominately Mn- and Fe-rich spessartine and almandine (Fig. 7), consistent with enrichment of Fe and Mn, e.g., Fe–Mn crust on the seafloor (Burton et al., 1999).
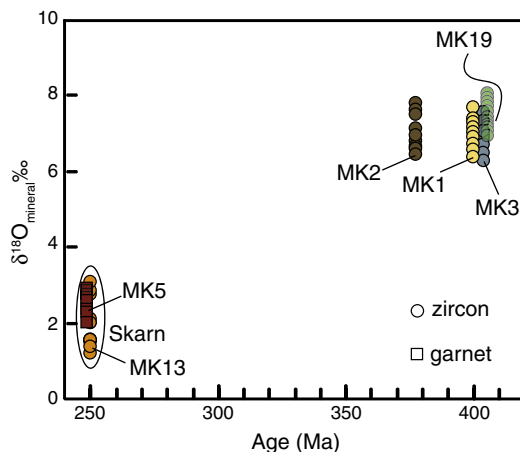
Moreover, the oxygen isotope compositions of zircons from the host rocks are very different from those of skarns. As such, the available geological, geochronological and isotopic data do not support the idea that the skarn formed coevally with the volcanic rocks, hence we believe the VMS model cannot explain the origin of the Mengku iron deposit.

4.2.2. Granite-generated skarn deposit?

In contrast to the VMS model which links a skarn with volcanism, the granite-generated skarn model considers that the skarn results from interaction between granite-related magmatic fluids and carbonate-rich wall rocks (Xu et al., 2010; Yang et al., 2010). Three types of
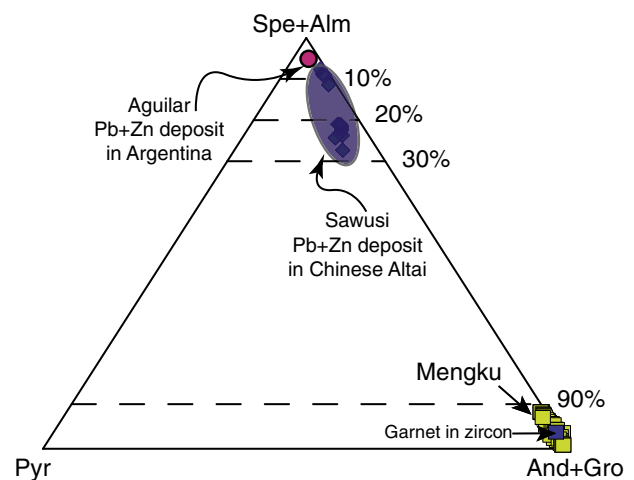

Fig. 6. Plot of age vs. oxygen isotope compositions of garnet and zircons.

Fig. 7. Ternary plots of garnet compositions from major skarn types. The open square are from the Mengku deposit, the diamonds are from Sawusi deposit and red circle from Aguilar deposit. End members: And: andradite, Gro: grossular, Pyr: pyrope, Spe: spessartine, Alm: almandine. The data for Sawusi are from Liu et al. (2010) and for Aguilar from Gemmell et al. (1992).

Table 3
Garnet compositions from the mineralized skarns in the Mengku iron deposit.

Sample	SiO$_2$	TiO$_2$	Al$_2$O$_3$	Cr$_2$O$_3$	Fe$_2$O$_3$	MnO	MgO	CaO	Total	Si	Ti	Al	Cr	Fe^{3+}	Fe^{2+}	Mn	Mg	Ca	Ura	And	Pyr	Spe	Gro	Alm
	wt.%									at.%									End-member proportions					
MK5A	37.24	0.01	6.01	<mdl	21.50	0.23	0.03	34.12	99.14	3.00	<mdl	0.57	<mdl	1.43	0.03	0.02	<mdl	2.95	<mdl	71.37	0.12	0.53	27.12	0.87
	36.95	<mdl	4.44	<mdl	24.61	0.38	0.04	32.64	99.06	3.01	<mdl	0.43	<mdl	1.57	0.11	0.03	<mdl	2.85	<mdl	78.60	0.15	0.87	16.70	3.69
	37.31	<mdl	5.00	<mdl	23.65	0.30	0.03	32.67	98.96	3.03	<mdl	0.48	<mdl	1.50	0.10	0.02	<mdl	2.84	<mdl	75.85	0.13	0.69	19.83	3.50
	36.94	0.06	3.72	<mdl	25.51	0.34	0.05	31.97	98.59	3.03	<mdl	0.36	<mdl	1.62	0.13	0.02	0.01	2.81	<mdl	81.82	0.20	0.79	12.80	4.39
MK5B	37.12	0.01	4.43	0.05	24.34	0.29	0.04	33.12	99.40	3.01	<mdl	0.42	<mdl	1.57	0.09	0.02	<mdl	2.88	0.15	78.60	0.15	0.66	17.57	2.86
	37.18	0.03	5.21	0.02	23.13	0.20	0.02	33.14	98.93	3.02	<mdl	0.50	<mdl	1.49	0.08	0.01	<mdl	2.88	0.05	74.88	0.06	0.46	21.78	2.76
	37.01	0.04	5.87	0.01	22.47	0.26	0.01	33.35	99.02	3.00	<mdl	0.56	<mdl	1.44	0.08	0.02	<mdl	2.90	0.04	71.94	0.03	0.58	24.59	2.82
	37.15	0.07	5.54	0.08	22.31	0.25	0.02	33.52	98.94	3.01	<mdl	0.53	<mdl	1.46	0.06	0.02	<mdl	2.91	0.24	73.16	0.07	0.58	24.08	1.87
MK6	37.05	<mdl	3.96	<mdl	24.00	0.19	0.02	33.43	98.65	3.02	<mdl	0.38	<mdl	1.60	0.04	0.01	<mdl	2.92	<mdl	80.78	0.09	0.43	17.49	1.21
	37.00	0.06	3.50	<mdl	25.73	0.33	0.03	32.07	98.72	3.03	<mdl	0.34	<mdl	1.64	0.12	0.02	<mdl	2.81	<mdl	82.92	0.13	0.76	12.01	4.17
	36.72	<mdl	3.57	<mdl	24.39	0.22	0.02	33.61	98.53	3.01	<mdl	0.35	<mdl	1.65	0.02	0.02	<mdl	2.95	<mdl	82.69	0.09	0.52	15.96	0.74
	37.14	<mdl	3.08	<mdl	25.34	0.23	0.04	33.17	99.00	3.03	<mdl	0.30	<mdl	1.68	0.05	0.02	<mdl	2.90	<mdl	85.05	0.15	0.54	12.69	1.57
MK7	36.96	0.05	2.98	<mdl	25.57	0.23	0.03	32.82	98.64	3.03	<mdl	0.29	<mdl	1.69	0.06	0.02	<mdl	2.88	<mdl	85.45	0.10	0.54	11.76	2.14
	37.47	<mdl	6.79	<mdl	20.49	0.33	<mdl	34.35	99.43	3.01	<mdl	0.64	<mdl	1.35	0.02	0.02	<mdl	2.95	<mdl	67.86	0.02	0.76	30.71	0.66
	36.93	0.12	3.51	<mdl	25.39	0.26	0.04	32.35	98.60	3.03	0.01	0.34	<mdl	1.64	0.10	0.02	0.01	2.84	<mdl	82.84	0.17	0.62	12.93	3.45
	37.18	<mdl	4.56	0.05	24.24	0.22	0.02	33.12	99.39	3.01	<mdl	0.44	<mdl	1.55	0.09	0.01	<mdl	2.88	0.16	77.96	0.09	0.50	18.23	3.07
MK9	37.12	0.02	3.10	0.04	26.32	0.41	0.02	32.40	99.43	3.03	<mdl	0.30	<mdl	1.68	0.11	0.03	<mdl	2.83	0.12	84.85	0.09	0.95	10.21	3.77
	36.79	0.02	2.39	0.05	26.60	0.26	0.03	32.47	98.61	3.03	<mdl	0.23	<mdl	1.74	0.09	0.02	<mdl	2.86	0.16	88.11	0.11	0.61	8.11	2.89
	36.40	0.62	4.58	<mdl	22.82	0.27	0.02	33.73	98.44	2.98	0.04	0.44	<mdl	1.55	0.01	0.02	<mdl	2.95	0.01	77.82	0.06	0.63	21.11	0.37
MK10	36.79	0.50	3.13	0.01	24.68	0.27	0.01	33.21	98.60	3.01	0.03	0.30	<mdl	1.67	0.02	0.02	<mdl	2.91	0.04	84.63	0.05	0.63	13.90	0.76
	36.78	0.34	5.14	0.02	22.87	0.24	0.01	33.18	98.58	3.00	0.02	0.49	<mdl	1.49	0.07	0.02	<mdl	2.90	0.07	75.10	0.02	0.56	22.02	2.23
	36.66	0.41	3.41	0.02	25.68	0.26	0.02	32.39	98.85	3.00	0.03	0.33	<mdl	1.65	0.11	0.02	<mdl	2.84	0.06	83.30	0.07	0.60	12.30	3.67
	36.76	0.36	4.94	0.01	23.56	0.22	0.03	33.10	98.98	2.99	0.02	0.47	<mdl	1.52	0.08	0.01	<mdl	2.89	0.04	76.20	0.11	0.50	20.31	2.84
	36.55	0.33	5.01	<mdl	23.47	0.35	0.02	32.55	98.28	2.99	0.02	0.48	<mdl	1.51	0.10	0.02	<mdl	2.86	<mdl	75.68	0.06	0.80	20.03	3.42
MK11	37.00	<mdl	5.43	0.02	22.64	0.26	0.04	33.74	99.13	3.00	<mdl	0.52	<mdl	1.48	0.05	0.02	<mdl	2.93	0.08	74.02	0.16	0.60	23.42	1.71
	36.51	0.03	2.83	0.01	25.82	0.20	0.05	32.86	98.31	3.01	<mdl	0.27	<mdl	1.72	0.06	0.01	0.01	2.90	0.03	86.19	0.22	0.47	10.96	2.14
	36.78	0.05	2.80	<mdl	26.56	0.29	0.01	31.87	98.36	3.03	<mdl	0.27	<mdl	1.70	0.13	0.02	<mdl	2.82	<mdl	86.25	0.05	0.68	8.73	4.29
	36.63	0.01	6.11	0.01	21.61	0.34	<mdl	33.97	98.68	2.98	<mdl	0.59	<mdl	1.43	0.04	0.02	<mdl	2.96	0.03	70.91	0.01	0.77	26.94	1.33
	36.66	0.05	2.78	0.01	26.95	0.25	0.04	31.82	98.56	3.02	<mdl	0.27	<mdl	1.71	0.14	0.02	0.01	2.81	0.03	86.34	0.18	0.58	8.03	4.84
MK12	36.44	0.02	0.71	<mdl	28.08	0.32	0.05	32.57	98.19	3.03	<mdl	0.07	<mdl	1.91	0.04	0.02	0.01	2.90	<mdl	96.49	0.22	0.75	1.15	1.39
	36.83	<mdl	3.83	<mdl	24.34	0.35	0.04	33.06	98.45	3.02	<mdl	0.37	<mdl	1.62	0.05	0.02	0.01	2.90	<mdl	81.41	0.17	0.81	15.94	1.67
	36.64	0.08	3.80	0.02	24.35	0.31	0.04	32.84	98.08	3.01	<mdl	0.37	<mdl	1.62	0.06	0.02	0.01	2.90	0.07	81.38	0.17	0.72	15.68	1.97
MK13	36.44	0.02	2.96	0.06	25.37	0.27	0.04	33.39	98.55	3.00	<mdl	0.29	<mdl	1.71	0.04	0.02	0.01	2.94	0.19	85.46	0.18	0.62	12.37	1.17
	36.71	<mdl	5.54	<mdl	21.57	0.32	0.02	34.39	98.55	2.99	<mdl	0.53	<mdl	1.47	<mdl	0.02	<mdl	3.00	<mdl	72.82	0.10	0.74	26.35	<mdl
	36.93	0.01	4.77	<mdl	22.69	0.27	<mdl	33.81	98.48	3.01	<mdl	0.46	<mdl	1.53	0.01	0.02	<mdl	2.95	<mdl	76.97	<mdl	0.63	21.91	0.49
MK14	36.65	0.04	5.92	<mdl	21.47	0.27	0.03	34.01	98.39	2.99	<mdl	0.57	<mdl	1.44	0.02	0.02	<mdl	2.97	<mdl	71.69	0.10	0.62	26.83	0.76
	37.44	<mdl	4.11	<mdl	24.16	0.32	0.04	33.26	99.33	3.03	<mdl	0.39	<mdl	1.59	0.05	0.02	<mdl	2.89	<mdl	80.18	0.17	0.75	17.16	1.75
	36.76	0.01	3.63	<mdl	24.56	0.31	0.04	32.98	98.29	3.02	<mdl	0.35	<mdl	1.64	0.05	0.02	<mdl	2.90	<mdl	82.33	0.15	0.72	15.06	1.74
Garnet in zircon in MK13	36.63	<mdl	2.13	<mdl	26.50	0.26	<mdl	32.63	98.15	3.03	<mdl	0.21	<mdl	1.77	0.06	0.02	<mdl	2.89	<mdl	89.51	0.02	0.60	7.83	2.04
	36.81	<mdl	1.62	0.02	26.95	0.30	0.02	32.80	98.52	3.04	<mdl	0.16	<mdl	1.82	0.04	0.02	<mdl	2.90	0.07	91.98	0.07	0.71	5.76	1.40
	36.94	<mdl	5.41	0.03	22.80	0.33	0.02	33.64	99.17	2.99	<mdl	0.52	<mdl	1.49	0.06	0.02	<mdl	2.92	0.10	74.11	0.08	0.74	22.98	1.99

<mdl — lower than the detecting limit. Number of ions on the basis of 12 atoms of oxygen and with Fe^{2+}/Fe^{3+} calculated assuming full site occupancy. Ura: uvarovite, And: andradite, Pyr: pyrope, Spe: spessartine, Gro: grossular, Alm: almandine.

granitic rocks are present in the Mengku mine area, two with an emplacement age of ca. 400 Ma (Yang et al., 2010), and one of ca. 380 Ma (Xu et al., 2010). Yang et al. (2008) and Xu et al. (2010) interpreted the ages of granites in the Mengku mine area (378 Ma and 400 Ma) to represent the time of granite emplacement and ore formation implying a granite-generated skarn model. However, this interpretation is contrary to geological evidence, as no contact relationship between granite and skarn can be observed either on the surface (Fig. 2), or in drill cores (FGTBGMRX, 2005). The strata located between the granites and skarn underwent strong deformation and low-grade metamorphism, and do not share the alteration textures of the skarn.

Some fluid inclusions with high salinities (up to 60.3 wt.% NaCl equiv.) and high homogenization temperatures (Th up to 550 °C) recorded from the Mengku deposit were interpreted as evidence of the granite-generated model (Xu et al., 2010; Yang et al., 2008). High Th inclusions were recorded in the garnet, whereas all the high salinity values were from fluid inclusions in quartz (Xu et al., 2010). The salinity values from fluid inclusions in garnet and diopside are lower than 13 wt.% NaCl equiv. (Xu et al., 2010). Therefore, we consider that these fluid inclusion data do not provide robust evidence to support a model of granite-related skarn, and in contrary suggest a typical metamorphic fluid affinity (<20 wt.%; Heinrich et al., 1992). Most importantly, our new in-situ zircon U–Pb age and oxygen isotopes do not support the granite-generated idea. The hydrothermal zircon ages are significantly younger than those of the granites (ca. 380 Ma), whereas hydrothermal zircon oxygen isotope ratios are consistent with those of garnet, but very different from all values of the granites in the mine area. If we assume that the hydrothermal zircon oxygen isotopes were generated by two different sources of assimilation, the volcanic wallrocks have $\delta^{18}O‰$ values of 7.0‰ to 8.0‰, hence a very depleted-O source is needed, not recorded in granites from the mine area.

As mentioned above, all igneous activity and the latest exhumation metamorphism terminated in the Early Permian in the Chinese Altai (Jahn et al., 2000; Wang et al., 2006; Wang et al., 2009b; Zheng et al., 2007). Granitoids with emplacement ages closest to 250 Ma have only been reported from Keketuohai (277 Ma, SHRIMP U–Pb, Wang et al., 2007), which is much older than our new Mesozoic ages and are more than 100 km from the Mengku mine, and their $\delta^{18}O$ value ranges from 7.4‰ to 12.2‰ (Kang and Wang, 1992). It is well known that granite-generated fluids can travel some distance from their source to interact with appropriate country rocks to produce a skarn (Meinert et al., 2005), however we do not believe that pluton-generated fluids can flow the distance required in this case. Moreover, the ore-forming fluids in Mengku are characterized by recycled low $\delta^{18}O$ isotope ratios. Nevertheless, we cannot exclude the possibility that there is a ca. 250 Ma granitic batholith deep beneath the Mengku iron deposit.

4.2.3. Strike–slip shear zone related?

Fluids and heat are necessary to produce skarns and associated ore deposits. Combining previous results with our work, the ore-forming fluids at the Mengku deposit cannot originate from any granites in the mine area or from ancient seawater. The Erqis Fault is the largest in Asia, and several lode gold deposits are located within the shear zone or along subsidiary, parallel, second- or third-order faults that formed in the Permian such as the Tesibahan and Abagong faults (Rui et al., 2002; Xu et al., 2008). The activation of the Abagong Fault system is consistent with movement of the Erqis Fault that has Th–Pb monazite age of 246 ± 18 Ma (Briggs et al., 2009). Pirajno (2010) proposed that many Cu–Ni and lode gold deposits that occur along major strike–slip faults with formation ages of 280–240 Ma in Central Asia may have resulted from upwelling of mantle material. There are also many Permian–Triassic ultramafic to mafic volcanic rocks along the Erqis and subsidiary faults in the Chinese Altai (Yuan et al., 2011; Zhang et al., 2010). Hence, the heat to form the skarn and ore deposits may be related to the upwelling of hot mantle material. Since the ore-forming fluids of the Mengku iron deposit have strong meteoric water signatures we propose

that the meteoric water was transported down a subduction zone, then mixed with fluids that was dehydrated by the upwelling of hot mantle, which produced low $\delta^{18}O$ fluids that were transferred up and along the Erqis shear zone and second-order faults during exhumation (Fig. 8), acting as conduits for heat and fluids. This resulted in metasomatism of carbonate-rich rocks in the hanging wall of the fault and creation of the skarn. Notably, it is common to observe skarn minerals in shear zones, as in the Ailao Shan strike–slip shear zone, SW China (Leloup and Kienast, 1993), and the Bancroft shear zone in Ontario, Canada (Mezger et al., 1993).

The Mengku deposit is not in the Erqis shear zone, but is located at the boundary between the Abagong thrust and in Devonian rocks of the Kangbutiebao Formation. We propose that the deep-origin fluids may have metasomatized the fertile and permeable lithologies of the Early Devonian rocks enriched in calcium, hence the ores are stratabound in the Early Devonian rhyolitic volcaniclastics (Fig. 8). As mentioned above, the Devonian volcanic rocks in Chinese Altai host many VMS deposits, which may have been enriched in iron during the extensive VMS mineralization in the Early Devonian in an intra-arc or back-arc basin setting (Wan et al., 2010a; Wan et al., 2010b). Based on the regional geological background, the Erqis Fault zone was able to act as a conduit for high temperature fluids, and the Devonian volcanic rocks may supply the iron to form the Mengku deposit.

4.3. Implications for orogenic ore deposits

Orogenic lode deposits are exclusively found in metamorphic terranes, whose principal characteristic is their strong structural control and close relation with major shear zones (Groves et al., 2003). The ore genesis of these orogenic lodes is attributed to the action of deep-circulating crustal fluids that may have been caused by devolatilization reactions or deep-seated magma (Goldfarb et al., 2005; Groves et al., 2003; Phillips and Powell, 2009; Pirajno, 2009). Therefore, the precise role of the igneous activity in the genesis of the mineralization remains uncertain for orogenic gold deposits, but all these ore deposits required the shear zone as a channel for the necessary fluids.

Many orogenic gold deposits form over wide range of temperatures from lower than 100 °C and up to ca. 500 °C, such as the Lupin gold deposit in the Archean Slave Province in northern Canada. At this deposit, gold is enclosed by skarns and located in a shear-zone, however was not related to intrusions near the mine (Bullis et al., 1994). The Hemlo gold–chromium–molybdenum deposit on the northeastern shore of Lake Superior, Canada is also an example of mineralization spatially associated with a shear zone (Pan et al., 1991). It is evident that shear zones are associated with fluids under a broad temperature range and are responsible for the generation of a variety of orogenic gold deposits such as Cu, Mo, Pb, Zn, Ag. However, other ore deposits with the same style as orogenic gold lode deposits have not been commonly reported in the international literatures. For example, Chen et al. (2004) described an orogenic silver deposit in the Qinling belt in China. In this study, we show that the Mengku iron deposit has a close spatial relationship with the regional Erqis shear zone, and for the first time we use the age of hydrothermal zircon to better constrain the mineralization age, and accordingly demonstrate a temporal relationship with the shear zone. Therefore, we propose that the formation of the Mengku deposit was genetically related to the shear zone, although we cannot completely evaluate the role of the associated magma. If the proposed model for the Mengku deposit is viable, then major shear zones can be an important target for skarn deposit research, as they are widely distributed in orogenic belts.

5. Conclusions

LA–ICP-MS analyses of zircon from host meta-rhyolitic volcaniclastic rocks (MK19) yield a $^{206}Pb/^{238}U$ weighted zircon age of 404 ± 5 Ma. Similar analysis on zircons from the mineralized skarn (MK13) yielded

Late Permian to Early Triassic

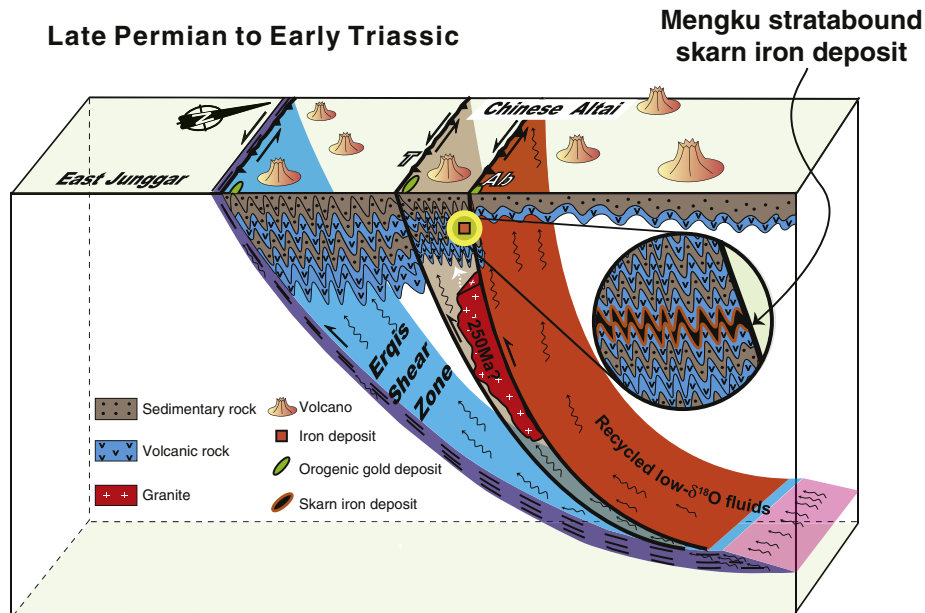**Mengku stratabound skarn iron deposit**

Fig. 8. Model of ore genesis of the Mengku deposit. Oblique thrust modified from Qu and Zhang (1994). T — Tesibahan Fault, Ab — Abagong Fault. See text for details.

a $^{206}Pb/^{238}U$ weighted zircon age of 250 ± 2 Ma. We consider that zircon separated from the mineralized skarn is of hydrothermal origin, as they contain skarn minerals and fluid inclusions. Thus, the date of the zircon represents the formation age of the skarn and associated iron mineralization. The hydrothermal age in the present study is not only significantly younger than that of ore-hosting strata (404 Ma), and that of granites (378 to 404 Ma) in the mine area, but is also younger than the latest regional igneous activity and metamorphism in the early Permian. The hydrothermal zircon are coeval with the activation of the major Erqis shear zone and associated upwelling of hot mantle material in the Permian to Triassic. The oxygen isotopes of the hydrothermal zircon are 2.3‰–3.0‰, which is consistent with the $\delta^{18}O$ of garnet (1.2‰–3.2‰) in skarns, but much lower than that of zircon (7.0‰–8.0‰) in volcanic wallrocks (MK19), or that of zircon from biotite granite (MK1, 6.4‰–7.5‰), two-mica granite (MK2, 6.4‰–7.8‰) and tonalite (MK3, 6.3‰–7.5‰) in the mine area. The fluids sources documented by the oxygen isotopes of garnet and hydrothermal zircon have strong signatures of meteoric water, but are very different from those of granite and volcanic rocks in the mine area. Combining our work with regional geological data, we propose that the ore formation was a result of metasomatism between Devonian Ca-rich volcaniclastic rocks and fluids mixed by meteoric water and mineral dehydration at depth in the Erqis shear zone. Our work provides new evidence that a major shear zone can act as a high temperature fluid conduit to produce an economically important iron deposit. Therefore, similar shear zones should be explored for iron deposits in the future.

References

Allen, M.B., Windley, B.F., Zhang, C., 1993. Palaeozoic collisional tectonics and magmatism of the Chinese Tien Shan, central Asia. Tectonophysics 220, 89–115.

Andersen, T., 2002. Correction of common lead in U–Pb analyses that do not report ^{204}Pb. Chem. Geol. 198, 59–79.

Appel, P.W.U., 1994. Stratabound scheelite in altered Archaean komatiites, West Greenland. Miner. Deposita 29, 341–352.

Black, L.P., Kamo, S.L., Allen, C.M., Davis, D.W., Aleinikoff, J.N., Valley, J.W., Mundil, R., Campbell, I.H., Korsch, R.J., Williams, I.S., Foudoulis, C., 2004. Improved $^{206}Pb/^{238}U$ microprobe geochronology by the monitoring of a trace-element-related matrix effect; SHRIMP, ID-TIMS, ELA–ICP-MS and oxygen isotope documentation for a series of zircon standards. Chem. Geol. 205, 115–140.

Briggs, S.M., Yin, A., Manning, C.E., Chen, Z.L., Wang, X.F., Grove, M., 2007. Late Paleozoic tectonic history of the Ertix Fault in the Chinese Altai and its implications for the development of the Central Asian Orogenic System. Geol. Soc. Am. Bull. 119, 944–960.

Briggs, S.M., Yin, A., Manning, C.E., Chen, Z.L., Wang, X.F., 2009. Tectonic development of the southern Chinese Altai Range as determined by structural geology, thermobarometry, $^{40}Ar/^{39}Ar$ thermochronology, and Th/Pb ion-microprobe monazite geochronology. Geol. Soc. Am. Bull. 121, 1381–1393.

Bullis, H.R., Hureau, R.A., Penner, B.D., 1994. Distribution of gold and sulfides at Lupin, Northwest Territories. Econ. Geol. 89, 1217–1227.

Burton, K.W., Bourdon, B., Birck, J.-L., Allègre, C.J., Hein, J.R., 1999. Osmium isotope variations in the oceans recorded by FeMn crusts. Earth Planet. Sci. Lett. 17, 185–197.

Chai, F., Mao, J., Dong, L, Yang, F., Liu, F., Geng, X., Zhang, Z., 2009. Geochronology of metarhyolites from the Kangbutiebao Formation in the Kelang basin, Altay Mountains, Xinjiang: implications for the tectonic evolution and metallogeny. Gondwana Res. 16, 189–200.

Charvet, J., Shu, L., Laurent-Charvet, S., 2007. Paleozoic structural and geodynamic evolution of eastern Tianshan (NW China): welding of the Tarim and Junggar plates. Episodes 30, 162–185.

Chen, B., Jahn, B.M., 2004. Genesis of post-collisional granitoids and basement nature of the Junggar Terrane, NW China: Nd–Sr isotope and trace element evidence. J. Asian Earth Sci. 23, 691–703.

Chen, Y.J., Pirajno, F., Sui, Y.H., 2004. Isotope geochemistry of the Tieluping silver–lead deposit, Henan, China: a case study of orogenic silver-dominated deposits and related tectonic setting. Miner. Deposita 39, 560–575.

Ciobanu, C.L., Cook, N.J., 2004. Skarn textures and a case study: the Ocna de Fier–Dognecea orefield, Banat, Romania. Ore Geol. Rev. 24, 315–370.

Clayton, R.N., Mayeda, T.K., 1963. The use of bromine pentafluoride in the extraction of oxygen from oxides and silicates for isotopic analysis. Geochim. Cosmochim. Acta 27, 43–52.

Cunningham, W.D., Windley, B.F., Dorjnamjaa, D., Badamgarov, G., Saandar, M., 1996. A structural transect across the Mongolian Western Altai: active transpressional mountain building in central Asia. Tectonics 15, 142–156.

Doyle, M.G., Allen, R.L., 2003. Subsea-floor replacement in volcanic-hosted massive sulfide deposits. Ore Geol. Rev. 23, 183–222.

Einaudi, M.T., Meinert, L.D., Newberry, R.J., 1981. Skarn deposits, Economic geology 75th Annniversary Volume, XXX-XXXX.

Fourth Geological Team of Bureau of Geology and Mineral Resources of Xinjiang (FGTBGMRX), 2005. Proposals for Deep Prospecting of the Mengku Iron Depsoit, Fuyun County, Xinjiang.

Franklin, J.M., Gibson, H.L., Galley, A.G., Jonasson, I.R., 2005. Volcanogenic massive sulfide deposits. In: Hedenquist, J.W., Thompson, J.F.H., Goldfarb, R.J., Richards, J.P. (Eds.), Economic Geology 100th Anniversary Volume, pp. 523–560.

Gemmell, J.B., Zantop, H., Meinert, L.D., 1992. Genesis of the Aguilar zinc–lead–silver deposit, Argentina; contact metasomatic vs. sedimentary exhalative. Econ. Geol. 87, 2085–2112.

Goldfarb, R.J., Mao, J.W., Hart, C., Wang, D.H., Anderson, E., Wang, Z.L., 2003. Tectonic and metallogenic evolution of the Altay Shan, Northern Xinjiang Uygur Autonomous region, Northwestern China. In: Mao, J.W., et al. (Ed.), Tectonic Evolution and Metallogeny of the Chinese Altay and Tianshan. Centre for Russian and Central Asian Mineral Studies, Natural History Museum, London, pp. 7–17.

Goldfarb, R.J., Baker, T., Dubé, B., Groves, D.I., Hart, C.J.R., Gosselin, P., 2005. Distribution, character, and genesis of gold deposits in metamorphic terranes. Economic Geology 100th Anniversary Volume, pp. 407–450.

Griffin, W.L., Powell, W.J., Pearson, N.J., OReilly, S.Y., 2008. GLITTER: data reduction software for laser ablation ICP MS. In: Sylvester, P.J. (Ed.), Laser Ablation–ICP MS in the Earth Sciences: Current Practices and Outstanding Issues, pp. 308–311.

Groves, D.I., Goldfarb, R.J., Robert, F., Hart, C.J.R., 2003. Gold deposits in metamorphic belts: overview of current understanding, outstanding problems, future research, and exploration significance. Econ. Geol. 98, 1–29.

Gu, L., Khin, Z., Hu, W., Zhang, K., Ni, P., He, J., Xu, Y., Lu, J., Lin, C., 2007. Distinctive features of Late Palaeozoic massive sulphide deposits in South China. Ore Geol. Rev. 31, 107–138.

Heinrich, C., Ryan, C., Mernagh, T., Eadington, P., 1992. Segregation of ore metals between magmatic brine and vapor; a fluid inclusion study using PIXE microanalysis. Econ. Geol. 87, 1566.

Hoskin, P.W.O., 2005. Trace-element composition of hydrothermal zircon and the alteration of Hadean zircon from the Jack Hills, Australia. Geochim. Cosmochim. Acta 69, 637–648.

Hoskin, P.W.O., Schaltegger, U., 2003. The composition of zircon and igneous and metamorphic petrogenesis. Rev. Mineral. Geochem. 53, 27–62.

Jackson, S.E., Pearson, N.J., Griffin, W.L., Belousova, E.A., 2004. The application of laser ablation–inductively coupled plasma-mass spectrometry to in situ U–Pb zircon geochronology. Chem. Geol. 211, 47–69.

Jahn, B.M., Wu, F.Y., Chen, B., 2000. Massive granitoid generation in central Asia: Nd isotope evidence and implication for continental growth in the Phanerozoic. Episodes 23, 82–92.

Johnson, M.C., Plank, T., 1999. Dehydration and melting experiments constrain the fate of subducted sediments. Geochem. Geophys. Geosyst. 1 (12), 1–26.

Kang, X., Wang, S., 1992. Characteristics of granites in Koktokay region, Xinjiang. Acta Petrol. Sin. 8, 399–404.

Kröner, A., Windley, B.F., Badarch, G., Tomurtogoo, O., Hegner, E., Jahn, B.M., Gruschka, S., Khain, E.V., Demoux, A., Wingate, M.T.D., 2007. Accretionary growth and crustformation in the central Asian Orogenic Belt and comparison with the Arabian–Nubian Shield. In: Hatcher, R.D., Carlson, M.P., McBride, J.H., Catalán, M. (Eds.), 4-D Framework of Continental Crust: Geological Society of America Memoir, 200, pp. 181–209.

Leloup, P.H., Kienast, J.-R., 1993. High-temperature metamorphism in a major strike–slip shear zone: the Ailao Shan–Red River, People's Republic of China. Earth Planet. Sci. Lett. 118, 213–234.

Li, X., Liu, Y., Li, Q., Guo, C., Chamberlain, K.R., 2009. Precise determination of Phanerozoic zircon Pb/Pb age by multicollector SIMS without external standardization. Geochem. Geophys. Geosyst. 10 (4), Q04010.

Li, Q., Li, X., Liu, Y., Tang, G., Yang, J., Zhu, W., 2010. Precise U–Pb and Pb–Pb dating of Phanerozoic baddeleyite by SIMS with oxygen flooding technique. J. Anal. At. Spectrom. 25, 1107–1113.

Liu, W., Liu, L.J., Liu, X.J., Shang, H.J., Zhou, G., 2010. Age of early Devonian Kangbutiebao Formation along the southern Altay Mountain and its northesatern extension. Acta Petrol. Sin. 26, 387–400.

Long, X.P., Sun, M., Yuan, C., Xiao, W.J., Lin, S.F., Wu, F.Y., Xia, X.P., Cai, K.D., 2007. U–Pb and Hf isotopic study of zircons from metasedimentary rocks in the Chinese Altai: implications for Early Paleozoic tectonic evolution. Tectonics 26. doi:10.1029/2007TC002128.

Long, X., Yuan, C., Sun, M., Xiao, W., Zhao, G., Wang, Y., Cai, K., Xia, X., Xie, L., 2010. Detrital zircon ages and Hf isotopes of the early Paleozoic flysch sequence in the Chinese Altai, NW China: new constrains on depositional age, provenance and tectonic evolution. Tectonophysics 480, 213–231.

Ludwig, K.R., 2001. Isoplot/Ex, rev. 2.49: A Geochronological Toolkit for Microsoft Excel, 1a. Berkeley Geochronological Center, Berkeley. 55 pp.

Maher, K.C., 2010. Skarn alteration and mineralization at Coroccohuayco, Tintaya District, Peru. Econ. Geol. 105, 263–283.

Meinert, L.D., Hefton, K.K., Mayes, D., Tasiran, I., 1997. Geology, zonation, and fluid evolution of the big Gossan Cu–Au skarn deposit, Ertsberg district: Irian Jaya. Econ. Geol. 92, 509–534.

Meinert, L.D., Dipple, G.M., Nicolescu, S., 2005. World skarn deposits. Economic Geology 100th Anniversary Volume, pp. 299–405.

Mezger, K., Essene, E.J., Pluijm, B.A., Halliday, A.N., 1993. U–Pb geochronology of the Grenville Orogen of Ontario and New York: constraints on ancient crustal tectonics. Contrib. Mineral. Petrol. 114, 13–26.

Mueller, A.G., 1997. The Nevoria gold skarn deposit in Archean iron-formation, Southern Cross greenstone belt, Western Australia; I, tectonic setting, petrography, and classification. Econ. Geol. 92, 181–209.

Niu, H., Sato, H., Zhang, H., Ito, J.i., Yu, X., Nagao, T., Terada, K., Zhang, Q., 2006. Juxtaposition of adakite, boninite, high-TiO$_2$ and low-TiO$_2$ basalts in the Devonian southern Altay, Xinjiang, NW China. J. Asian Earth Sci. 28, 439–456.

Pan, Y., Fleet, M.E., Stone, W.E., 1991. Skarn mineralization (Cr, Fe, Au) in an Archean greenstone belt, White River Property, Hemlo area, Ontario. Econ. Geol. 86, 1626–1645.

Phillips, G.N., Powell, R., 2009. Formation of gold deposits: review and evaluation of the continuum model. Earth Sci. Rev. 94, 1–21.

Pirajno, F., 2009. Hydrothermal Processes and Mineral System. Springer Press, Perth, Australia. 1250 pp.

Pirajno, F., 2010. Intracontinental strike–slip faults, associated magmatism, mineral systems and mantle dynamics: examples from NW China and Altay–Sayan (Siberia). J. Geodyn. 50, 325–346.

Pons, J.M., Franchini, M., Meinert, L., Recio, C., Etcheverry, R., 2009. Iron skarns of the Vegas Peladas District, Mendoza, Argentina. Econ. Geol. 104, 157–184.

Qu, G., Zhang, J., 1994. Oblique thrust systems in the Altay orogen, China. J. Southeast Asian Earth Sci. 9, 277–287.

Raith, J.G., Stein, H.J., 2000. Re–Os dating and sulfur isotope composition of molybdenite from tungsten deposits in western Namaqualand, South Africa: implications for ore genesis and the timing of metamorphism. Miner. Deposita 35, 741–753.

Rui, Z.Y., Goldfarb, R., Qiu, Y.M., Zhou, T.H., Chen, R.Y., Pirajno, F., Yun, G., 2002. Paleozoic–early Mesozoic gold deposits of the Xinjiang Autonomous Region, northwestern China. Miner. Deposita 37, 393–418.

Sengör, A.M.C., Natal'in, B.A., 1996. Paleotectonics of Asia: fragments of a synthesis. In: Yin, A., Harrison, M. (Eds.), The Tectonic Evolution of Asia. Cambridge University Press, Cambridge, pp. 486–640.

Sengör, A.M.C., Natal'in, B.A., Burtman, V.S., 1993. Evolution of the Altaid tectonic collage and Palaeozoic crustal growth in Eurasia. Nature 364, 299–307.

Sun, M., Yuan, C., Xiao, W., Long, X., Xia, X., Zhao, G., Lin, S., Wu, F., Kroner, A., 2008. Zircon U–Pb and Hf isotopic study of gneissic rocks from the Chinese Altai: progressive accretionary history in the early to middle Palaeozoic. Chem. Geol. 247, 352–383.

Valley, J.W., 2003. Oxygen isotopes in zircon. Rev. Mineral. Geochem. 53, 343–385.

Wan, B., Zhang, L., Xiao, W., 2010a. Geological and geochemical characteristics and ore genesis of the Keketale VMS Pb–Zn deposit, Southern Altai Metallogenic Belt, NW China. Ore Geol. Rev. 37, 114–126.

Wan, B., Zhang, L.C., Xiang, P., 2010b. The Ashele VMS-type Cu–Zn deposit in Xinjiang, NW China formed in a rifted arc setting. Resour. Geol. 60, 150–164.

Wan, B., Xiao, W.J., Zhang, L.C., Windley, B., Han, C.M., Quinn, C., 2011. Contrasting styles of mineralization in the Chinese Altai and East Junggar. NW China: implications for the accretionary history of the southern Altaids. J. Geol. Soc. Lond. 168. doi:10.1144/0016-76492011-021.

Wang, Y.W., Wang, J.B., Wang, S.L., Ding, R.F., Wang, L.J., 2003. Geology of the Mengku iron deposit, Xinjing, China: a metamorphosed VMS? In: Mao, J.W., et al. (Ed.), Tectonic Evolution and Metallogeny of the Chinese Altay and Tianshan. Centre for Russian and Central Asian Mineral Studies, Natural History Museum, London, pp. 181–200.

Wang, T., Hong, D.W., Jahn, B.M., Tong, Y., Wang, Y.B., Han, B.F., Wang, X.X., 2006. Timing, petrogenesis, and setting of Paleozoic synorogenic intrusions from the Altai Mountains, Northwest China: implications for the tectonic evolution of an accretionary orogen. J. Geol. 114, 735–751.

Wang, T., Tong, Y., Jahn, B.M., Zou, T.R., Wang, Y.B., Hong, D.W., Han, B.F., 2007. SHRIMP U–Pb zircon geochronology of the Altai No. 3 Pegmatite, NW China, and its implications for the origin and tectonic setting of the pegmatite. Ore Geol. Rev. 32, 325–336.

Wang, T., Jahn, B.M., Kovach, V.P., Tong, Y., Hong, D.W., Han, B.F., 2009a. Nd–Sr isotopic mapping of the Chinese Altai and implications for continental growth in the Central Asian Orogenic Belt. Lithos 110, 359–372.

Wang, W., Wei, C., Wang, T., Lou, Y., Chu, H., 2009b. Confirmation of pelitic granulite in the Altai orogen and its geological significance. Chin. Sci. Bull. 54, 2543–2548.

Wei, C., Clarke, G., Tian, W., Qiu, L., 2007. Transition of metamorphic series from the Kyanite- to andalusite-types in the Altai orogen, Xinjiang, China: evidence from petrography and calculated KMnFMASH and KFMASH phase relations. Lithos 96, 353–374.

Wiedenbeck, M., AllÉ, P., Corfu, F., Griffin, W.L., Meier, M., Oberli, F., Quadt, A.V., Roddick, J.C., Spiegel, W., 1995. Three natural zircon standards for U–Th–Pb, Lu–Hf, trace element and REE analyses. Geostand. Newsl. 19, 1–23.

Wilde, S.A., Valley, J.W., Peck, W.H., Graham, C.M., 2001. Evidence from detrital zircons for the existence of continental crust and oceans on the Earth 4.4 Gyr ago. Nature 409, 175–178.

Windley, B.F., Kröner, A., Guo, J.H., Qu, G.S., Li, Y.Y., Zhang, C., 2002. Neoproterozoic to Paleozoic geology of the Altai Orogen, NW China: new zircon age data and tectonic evolution. J. Geol. 110, 719–737.

Windley, B.F., Alexeiev, D., Xiao, W.J., Kröner, A., Badarch, G., 2007. Tectonic models for accretion of the Central Asian Orogenic Belt. J. Geol. Soc. Lond. 164, 31–47.

Xiao, W.J., Windley, B.F., Huang, B.C., Han, C.M., Yuan, C., Chen, H.L., Sun, M., Sun, S., Li, J.L., 2009a. End-Permian to mid-Triassic termination of the accretionary processes of the southern Altaids: implications for the geodynamic evolution, Phanerozoic continental growth, and metallogeny of Central Asia. Int. J. Earth Sci. 98, 1189–1217.

Xiao, W.J., Windley, B.F., Yuan, C., Sun, M., Han, C.M., Lin, S.F., Chen, H.L., Yan, Q.R., Liu, D.Y., Qin, K.Z., Li, J.L., Sun, S., 2009b. Paleozoic multiple subduction–accretion processes of the southern Altaids. Am. J. Sci. 309, 221–270.

Xiao, W., Huang, B., Han, C., Sun, S., Li, J., 2010. A review of the western part of the Altaids: a key to understanding the architecture of accretionary orogens. Gondwana Res. 18, 253–273.

Xie, L.W., Zhang, Y.B., Zhang, H.H., Sun, J.F., Wu, F.Y., 2008. In situ simultaneous determination of trace elements, U–Pb and Lu–Hf isotopes in zircon and baddeleyite. Chin. Sci. Bull. 53, 1565–1573.

Xu, J., Ding, R., Xie, Y., Zhong, C., Shan, L., 2008. The source of hydrothermal fluids for the Sarekoubu gold deposit in the southern Altai, Xinjiang, China: evidence from fluid inclusions and geochemistry. J. Asian Earth Sci. 32, 247–258.

Xu, L., Mao, J., Yang, F., Zheng, J., 2010. Geology, geochemistry and age constraints on the Mengku skarn iron deposit in Xinjiang Altay, NW China. J. Asian Earth Sci. 39, 423–440.

Yang, F.Q., Mao, J.W., Chai, F.M., Liu, F., Zhou, G., Geng, X.X., Liu, G.R., Xu, L.G., 2008. Ore-forming fluids and metallogenesis of Mengku iron deposit in Altay, Xinjiang, China. Miner. Deposits 27, 659–678 (in Chinese with English abstract).

Yang, F., Mao, J., Liu, F., Chai, F., Guo, Z., Zhou, G., Geng, X., Gao, J., 2010. Geochronology and geochemistry of the granites from the Mengku iron deposit, Altay Mountains, northwest China: implications for its tectonic setting and metallogenesis. Aust. J. Earth Sci. 57, 803–818.

Yuan, C., Sun, M., Xiao, W., Li, X., Chen, H., Lin, S., Xia, X., Long, X., 2007. Accretionary orogenesis of the Chinese Altai: insights from Paleozoic granitoids. Chem. Geol. 242, 22–39.

Yuan, C., Sun, M., Xu, Y., Zhao, G.C., Xiao, W., Long, X.P., Yin, J.Y., 2011. Oceanic lithospheric mantle beneath the continental crust of the Chinese Altai. J. Geol. Soc. 168, 995–1000.

Zhang, C.L., Li, Z.X., Li, X.H., Xu, Y.G., Zhou, G., Ye, H.M., 2010. A Permian large igneous province in Tarim and Central Asian orogenic belt, NW China: results of a ca. 275 Ma mantle plume? Geol. Soc. Am. Bull. 122, 2020–2040.

Zheng, C., Kato, T., Enami, M., Xu, X.C., 2007. CHIME monazite ages of metasediments from the Altai orogen in northwestern China: Devonian and Permian ages of metamorphism and their significance. I Arc 16, 598–604.

Zonenshain, L.P., Kuzmin, M.I., Natapov, L.M. (Eds.), 1990. Geology of the USSR: A Plate-Tectonic Synthesis. American Geophysical Union, Washington D.C.. 242 pp.